View Online / Journal Homepage / Table of Contents for this issue
Dynamic Article Links

Journal of
Materials Chemistry

Cite this: *J. Mater. Chem.*, 2012, **22**, 17037

www.rsc.org/materials

PAPER

Robustly nano-tailored honeycomb structure for high-throughput antireflection polymer films†

Kiwoon Choi,‡[a] Sung Ho Park,‡[a] Young Min Song,[b] Chongdu Cho[c] and Han Sup Lee*[a]

Received 29th April 2012, Accepted 2nd July 2012
DOI: 10.1039/c2jm32706f

Downloaded by University of Illinois - Urbana on 21 September 2012
Published on 04 July 2012 on http://pubs.rsc.org | doi:10.1039/C2JM32706F

Although recently fabricated biomimetic nanostructures exhibit superior performance compared to corresponding nanostructures found in nature, their practical applications are limited due to the low mechanical stability of the nanostructures and the low productivity of the fabrication processes developed thus far. A nanoporous honeycomb structure that can alleviate any concentrated stress effectively was fabricated using roll-to-roll processable thermal nanoimprint lithography for high throughput and performance antireflection polymer films. A nanoscale positive (convex) antireflective structure of the moth eye, which shows broadband and omnidirectional antireflection properties, and a negative (concave) antireflective structure were produced using this process. The new nanoporous honeycomb structure exhibited high performance AR and enhanced mechanical stability. Moreover, a continuous process that can be used for industrial mass production was developed.

1. Introduction

Nano-scientists have been obtaining inspiration and design principles from the various nanotechnologies that exist in nature such as the superhydrophobicity of the lotus leaf, dry adhesion of the gecko's foot, attractive color of the butterfly's wing, and antireflection property of the moth's eye. Furthermore, artificial biomimetic materials produced based on the recent nanotechnologies might show properties that are even superior to the corresponding ones in nature.[1–5] But their practical applications are limited due to the low mechanical stability of the nanostructures and the low productivity of the fabrication processes developed thus far. These two common drawbacks have to be overcome for the further development of currently associated nanotechnologies.

AR coatings have been used extensively to enhance the optical performance of various optical components requiring increased transmittance, improved contrast and reduced surface glare and considerable efforts have been paid recently to further improve the AR performance. On the compound eyes of some nocturnal insects (moths and some butterflies) are positive (convex) antireflective structures (P-ARSs) of sub-300 nm size in non-close-packed nipple arrays. The ARS ensures the optical impedance matching at two interfaces (air–ARS and ARS–substrate), which is possible with the gradual reflective index (RI) profile along the normal direction of the substrate. In contrast to the conventional AR coatings, artificial ARSs biomimicking the compound eyes were theoretically predicted to show broadband AR behavior of up to one order of magnitude and omnidirectional AR for an incidence angle of up to 80 degrees.[6]

Since the performance of an AR film having a P-ARS on the surface can be controlled by various tunable parameters such as period, height, and shape of the ARS, high performance AR behavior can be obtained by carefully combining those parameters.[7–9] According to the theoretical analysis, it is possible to have an ideal AR performance showing the widest possible bandwidth and almost omnidirectional AR property when the ARS has fine period, very long size, and continuously tapered shape from the top (air side) to the bottom (substrate side).[1] However, it is almost impossible to have a vertically standing ARS if a flexible material like a polymer is used to make ARS of very high aspect ratio. The performance of an ARS is sensitively determined by the shape of the ARS especially when the height of the ARS is relatively short. In the case of a short ARS, the shape of the ARS, therefore, has to be elaborately controlled to ensure the desired ideal RI profile predicted by the theoretical calculation. Recently, a nanotailoring technique for the monolithic ARS structure on a polymethylmethacrylate (PMMA) substrate has been reported and high performance AR property was experimentally confirmed by establishing a liner RI profile in the ARS layer which was achieved by the short (about 200 nm) P-ARS on PMMA.[10]

It is important to maintain high mechanical stability of the P-ARS fabricated on the AR film because the ARS layer can be

[a]*Department of Advanced Fiber Engineering, Inha University, 253 Young-hyun-dong, Nam-gu, Incheon, 402-751, Republic of Korea. E-mail: hslee@inha.ac.kr; Fax: +82-32-876-0193; Tel: +82-32-860-8841*
[b]*Department of Materials Science and Engineering, University of Illinois at Urbana Champaign, Urbana, Illinois 61801, USA*
[c]*Department of Mechanical Engineering, Inha University, 253 Young-hyun-dong, Nam-gu, Incheon, 402-751, Republic of Korea*
† Electronic supplementary information (ESI) available. See DOI: 10.1039/c2jm32706f
‡ K.C., S.H.P contributed equally to this work.

exposed to external environments in many practical applications. Even though the P-ARS has been frequently fabricated to obtain high AR performance, its low mechanical stability has been a key drawback to be overcome for the practical application of AR products.[10–14] In the case of macroscopic physics, structures such as truss, honeycomb and dome are typical examples that effectively redistribute the stress concentrated on a certain point of the structure to secure high mechanical stability while maintaining the specific original function.[15,16] In this study, a macroscopic design technology was applied to nanoscale structure fabrication to enhance the mechanical stability of polymeric nanostructures necessary for the high throughput and performance of AR surfaces.

2. Results and discussion

2.1. Optical and mechanical calculation

The AR performance is inevitably affected by the RI profile of the interphase, which is determined by the precise structure of the ARS, *i.e.* period, height (or depth) and shape of the ARS.[7–9] Provided that the RI profile in the interphase layer is identical, different ARS morphologies can give the same AR behavior. Fig. 1a and b show two different ARSs of the solid of revolution shape, P-ARS and negative antireflective structure (N-ARS), respectively. As long as the period (d) of ARS is sufficiently smaller than the wavelength of incident light in the medium (λ/n), the effective RI (n_{eff}) of any depth (z) can be approximated by

$$n_{\text{eff}}(z) = \{f_{\text{bulk}}(z)n_{\text{bulk}}{}^{2/3} + [1 - f_{\text{bulk}}(z)]n_{\text{air}}{}^{2/3}\}^{3/2} \quad (1)$$

Here, $f_{\text{bulk}}(z)$ is the bulk material fraction at any depth (z), and n_{bulk} and n_{air} are the RI of the bulk material and air, respectively.[8,9] By controlling the $f_{\text{bulk}}(z)$ at any height of the P-ARS to be identical to the corresponding depth of the N-ARS, it is possible to have the same RI profiles along the normal direction in the interphase of the P-ARS and N-ARS layers. Both the P-ARS and N-ARS are optically identical as far as the AR performance is concerned. As confirmed in Fig. 1a, each P-ARS is isolated from the neighboring ARSs. On the other hand, each hole in N-ARS in Fig. 1b is "interconnected" structurally to all the holes in the hexagonal lattice through the bulk material. Since a mechanical stress applied to any point of the N-ARS structure can be redistributed to the neighboring holes in a nanoscale honeycomb structure, a higher mechanical stability of the N-ARS structure can be expected.[15,17]

To fabricate a N-ARS with high AR performance experimentally, it is essential to calculate theoretically the expected reflectance and transmittance from ARSs of various periods and depths. The ARS shape ensuring a linear RI profile in the ARS layer was reported to be one of the best structures in terms of its relatively low surface reflectance.[9,10] A model surface was designed with ARSs in a hexagonal lattice of 200 nm, which is small enough not to have any significant Mie and Rayleigh scattering at visible wavelengths.[8,18] The reflectance from that model surface showing a linear RI profile in the ARS layer was calculated using the rigorous coupled-wave analysis (RCWA) method.[19] Figure 1c shows the result for an ARS height up to 400 nm and over the range of visible wavelengths. As shown in the inset of Fig. 1c, the mean reflectance initially decreases rapidly and reaches approximately 0.1% at an ARS depth/height of 200 nm. Slight increases in reflectance have been observed with further increases in ARS depth/height to approximately 310 nm. In this study, an ARS depth/height of 200 nm was selected as a target value to maintain a low surface reflectance.

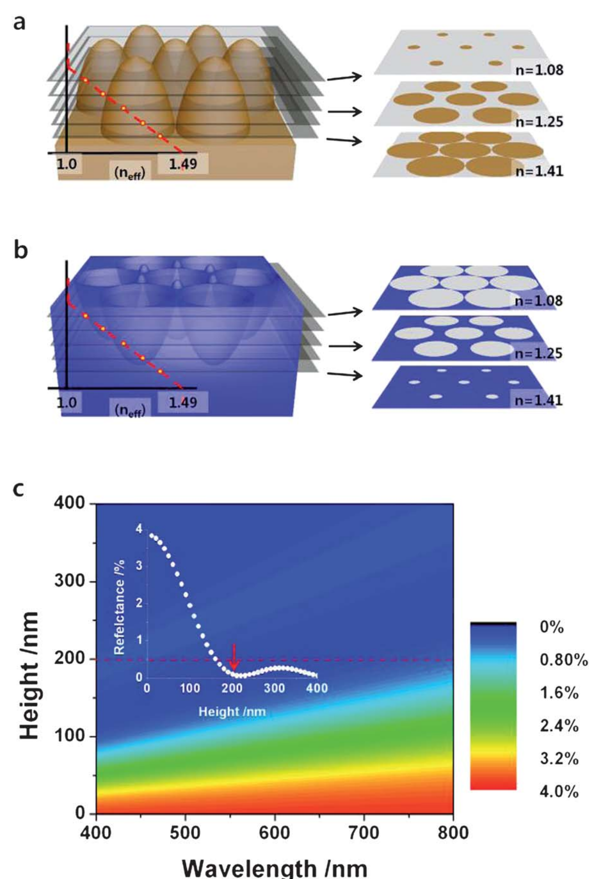

Fig. 1 (a and b), Schematic shapes of a P-ARS (a) and a N-ARS (b) showing an identical refractive index profile inside the interphase layer. The refractive index at any position along the normal direction of the film is plotted as a red dotted line. The area covered by the material and the resultant refractive index in three selected layers are also displayed. (c) Calculated reflectance from one surface showing a linear RI profile in (a) and (b) is displayed as a function of the wavelength for an ARS height of up to 400 nm. Mean reflectance as a function of the ARS height is also included.

The mechanical stabilities of both P-ARS and N-ARS were calculated numerically using the finite element method.[20] Fig. 2a shows the changes in morphology of P-ARS and N-ARS occurring during increasing normal stress. Fig. 2b presents the resulting stroke–stress curves obtained. As expected, N-ARS can be confirmed to undergo relatively smaller deformation for the same normal stress, compared to the corresponding P-ARS sample.

2.2. N-ARS fabrication with a RTNIL

The roll-to-roll thermal nanoimprint lithography (RTNIL) can be an efficient process for making a monolithic nanoporous N-ARS on a thermoplastic surface with high-throughput.[21–23] The production of a special roller mold is essential for making

Downloaded by University of Illinois - Urbana on 21 September 2012
Published on 04 July 2012 on http://pubs.rsc.org | doi:10.1039/C2JM32706F

 This journal is © The Royal Society of Chemistry 2012

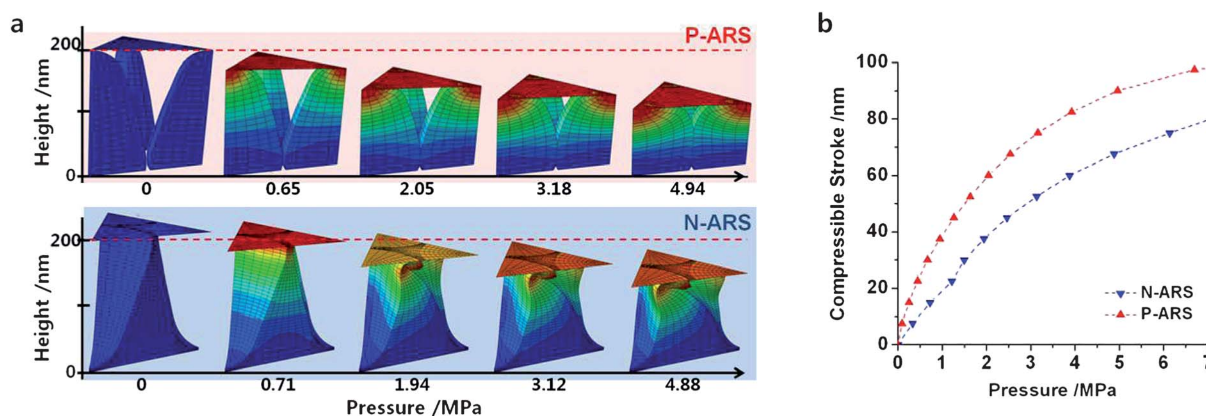

Fig. 2 Finite element analysis results of P-ARS and N-ARS. The structure changes in P-ARS (up) and N-ARS (down) occurring during the application of normal stress (a) and the resulting stroke–stress curves (b).

Downloaded by University of Illinois - Urbana on 21 September 2012
Published on 04 July 2012 on http://pubs.rsc.org | doi:10.1039/C2JM32706F

continuous roll-to-roll imprinting possible. The polymer film with the desired ARS on its surface needs to be sufficiently flexible to be wound around the circular roller. Moreover, the ARS itself needs to have a sufficiently high modulus, strength, and thermal stability to imprint its structure precisely onto a molten poly(methyl methacrylate) (PMMA) surface. Furthermore, it should have a low thermal expansion coefficient to minimize the deformation caused by the temperature change during the imprinting process, and also needs to have a low surface free energy for clean mold release from the imprinted PMMA surface.[23,24] Although polyimide (PI) has a relatively high surface energy (38.9 dyne per cm) compared to fluoropolymers or polydimethylsiloxane, which are typically low surface energy materials, it has a very high modulus (3.2 GPa), strength (75–90 MPa), and glass transition temperature (>400 °C) and a very low thermal expansion coefficient (5.5×10^{-5} K^{-1}). In this study, PI was used as a roller mold material because it has many of the desired thermal and mechanical properties essential for the RTNIL process during which high temperatures and pressures are experienced. For clean mold release, the surface area of the PI mold was kept as small as possible by forming an ARS with a minimum permissible height showing high AR performance.[25] As shown in Fig. 1c, an ARS with 200 nm depth and period was chosen as the target value for the experimental fabrication of an ARS. The ARS with an aspect ratio of one was expected to show enhanced mechanical durability (see the ESI† for details).

Multilayer anodized aluminum oxide (AAO) containing a tapered pore array in its pseudo-hexagonal lattice was initially prepared using a multistep anodization process, the schematic of which is shown in Fig. 3a.[26] The shape of the ARS (and $f_{\mathrm{bulk}}(z)$ eventually) can be tailored at any depth of the ARS layer to ensure the desired RI profile by carefully controlling the anodization and etching time in each step of the multistep anodization process.[10] By increasing the number of steps in the multistep anodization process, the shape of the pores in AAO approaches that of the continuously tapered morphology, as shown in the last figure in Fig. 3a (see ESI† and ref. 10 for details). Fig. 3b shows the top and side view images of the AAO template fabricated using the 5-step anodization and etching process. The tapered pore shape in the multilayer AAO could be confirmed. Both the pore depth and average value of the broadly distributed period were approximately 200 nm, which is consistent with the target value suggested by prior theoretical calculations. In addition, the intersections in a pseudo-hexagonal lattice are elevated slightly (by approximately 20 nm) from the common base plate, as indicated by the arrow in Fig. 3b.

A flexible PI mold with a positive structure on its surface was prepared by a template wetting process using a multilayer AAO template, the schematic diagram of which is shown in Fig. 3c. The pores in multilayer AAO could be filled with the PI precursor (Aldrich) using the difference in the surface tension between the aluminum oxide wall (solid) and imide precursor (liquid).[27,28] Upon thermosetting the precursor in the pores, a flexible PI mold was obtained by separating mechanically from multilayer AAO. Since this replicated PI mold could be prepared repeatedly using an identical multilayer AAO, the RTNIL used in this study might be an economical process for keeping the master multilayer AAO mold intact.[29] Fig. 3d shows the top and side scanning electron microscopy (SEM) images of the PI mold with a positive structure on its surface. Both the period (top view) and height of the tapered positive structure (side view) in a pseudo-hexagonal pattern were approximately 200 nm. The tapered pore array in the multilayer AAO appeared to be transferred almost precisely to the positive structure in the PI mold. Note that most of the positive structure stands vertically on the surface, possibly due to the relatively low aspect ratio. The PI mold film, approximately 5 cm in diameter, fabricated in this study, was wrapped around a stainless steel roller.

Fig. 3e shows a schematic diagram of the RTNIL process used in this work to fabricate the N-ARS AR film. The stainless steel roller was initially wound with a soft polydimethylsiloxane (PDMS) film to improve contact between the PMMA (M_w = 100 000 g mol^{-1}, Polysciences) film and the PI mold film, which was wrapped on top of the PDMS surface. The roller mold was pressed against and rotated on the PMMA film surface, which was preheated to above its glass transition temperature (105 °C). The PMMA film with the imprinted N-ARS on its surface was rotated and advanced with the roller, and then cooled with cold air before being demolded. Clean mold release was possible without any additional surface treatment of the PI mold probably because the positive structure on the PI film has a relatively

View Online

Downloaded by University of Illinois - Urbana on 21 September 2012
Published on 04 July 2012 on http://pubs.rsc.org | doi:10.1039/C2JM32706F

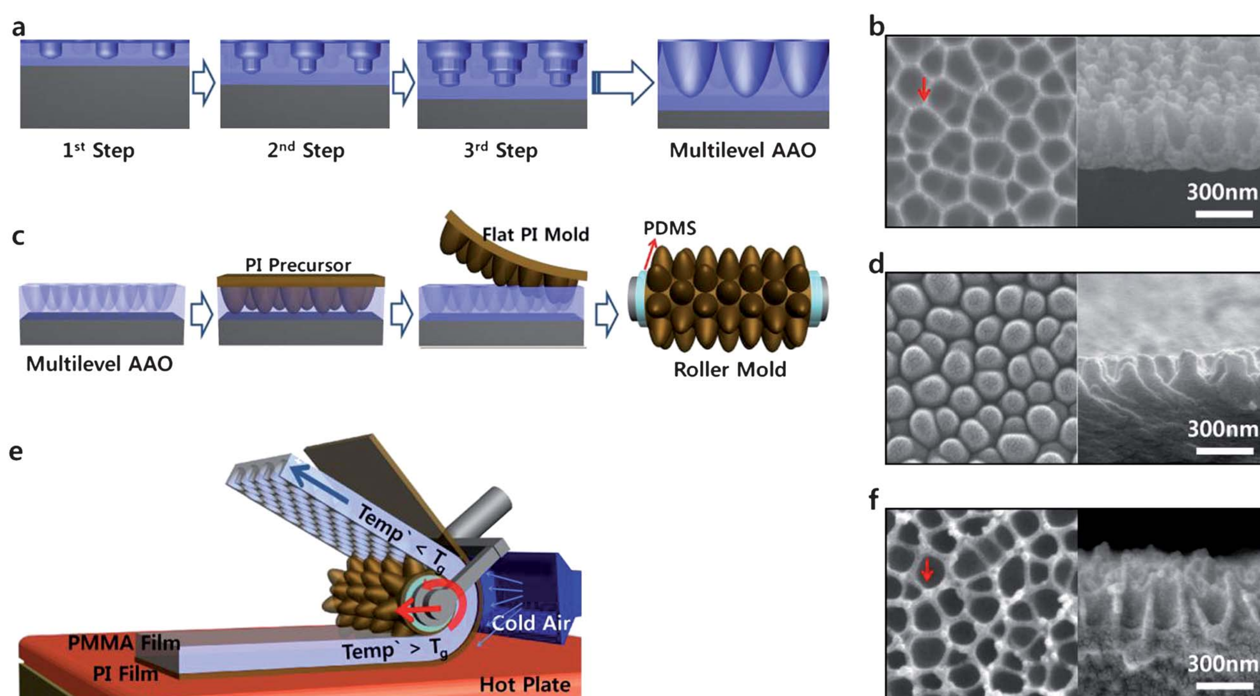

Fig. 3 (a) Multistep anodization and etching process for the fabrication of multilayer AAO with continuously tapered pores. (b) Top and side SEM images of the pores in multilayer AAO. (c) Schematic process to prepare a PI roller mold. The pores in multilayer AAO were filled with a PI precursor. After thermosetting, a flat PI mold film was detached from the AAO. The PI mold film was wound around a stainless cylinder, which had been covered with a thin PDMS film. (d) Top and side SEM images of the positive structures in a PI mold film. (e) Schematic diagram showing the roll-to-roll processable, thermal nanoimprint lithography used to prepare the N-ARS on a PMMA surface. (f) Top and side SEM images of the pores in the PMMA AR film. The red arrows in (b) and (f) correspond to the slightly elevated spots at the intersections of neighboring pores.

low aspect ratio, which serves to minimize the contact area between the PI mold and PMMA film.[25,30] Fig. 3f shows the top and side views of the imprinted PMMA film with N-ARS on its surface. The tapered porous morphology of N-ARS was confirmed, and the depth and mean period of N-ARS were approximately 200 nm, as expected. The slightly depressed areas at the intersection points in the pseudo-hexagonal lattice (denoted with the arrow in Fig. 3f) appear to correspond to the slightly elevated points in the multilayer AAO master template (see the arrow in Fig. 3b). This suggests that the imprinted PMMA film with N-ARS is a conjugate copy of the PI film with positive structures, and the tapered pore array in the multilayer AAO master template is transferred almost precisely to the N-ARS in the PMMA film.

2.3. Optical property of ARS films

The AR performance was evaluated by measuring the total reflectance (with an 8° incidence angle) and transmittance (normal incidence) of the imprinted PMMA film with N-ARS on one surface. Fig. 4a shows the reflectance results. Data obtained from the corresponding AR film with P-ARSs on one PMMA surface and from a flat PMMA film are also included in the figure for comparison (see ESI† for preparation of the P-ARS PMMA film). The reflectance data calculated based on the theoretical models shown in Fig. 1c are also included.

As expected from the theoretical prediction (approximately 3.9% reflectance from one PMMA flat surface), the reflectance from the flat reference sample with two flat surfaces was somewhere between 6.5% and 7.5% for a wavelength range from 400 nm to 800 nm. On the other hand, the corresponding mean reflectance of the N-ARS and P-ARS films was approximately 4.19%. Considering the 3.9% reflectance from one flat surface, the reflectance only from one ARS surface (either P-ARS or N-ARS films) would be approximately 0.29%, which is significantly smaller than that from the flat surface. As expected, very similar AR performance was observed from two different samples with identical RI profiles in the ARS layer despite their different ARS morphologies.

The AR performance was also evaluated by measuring the transmittance. As shown in Fig. 4b, the transmittance of a flat PMMA film ranged from approximately 92 to 93% over the visible wavelength range. On the other hand, the film with the N-ARS and P-ARS showed a mean transmittance of 95.5% and 95.55%, respectively. The data of both (N-ARS and P-ARS) correspond to approximately 98.8% transmittance provided that identical ARS structures were formed on both (front and back) surfaces. The slight difference between the theoretical and two experimental values especially at low wavelengths might be due to the small absorption of PMMA, which was neglected during RCWA calculation.

The transmittance was also measured as a function of the incidence angle at 525 nm with N-ARS, P-ARS, and flat films, and the results are shown in Fig. 4c. Compared to the flat reference film, the ARS films showed greater improvement in the AR performance over all wavelengths and incidence angles

 This journal is © The Royal Society of Chemistry 2012

Downloaded by University of Illinois - Urbana on 21 September 2012
Published on 04 July 2012 on http://pubs.rsc.org | doi:10.1039/C2JM32706F

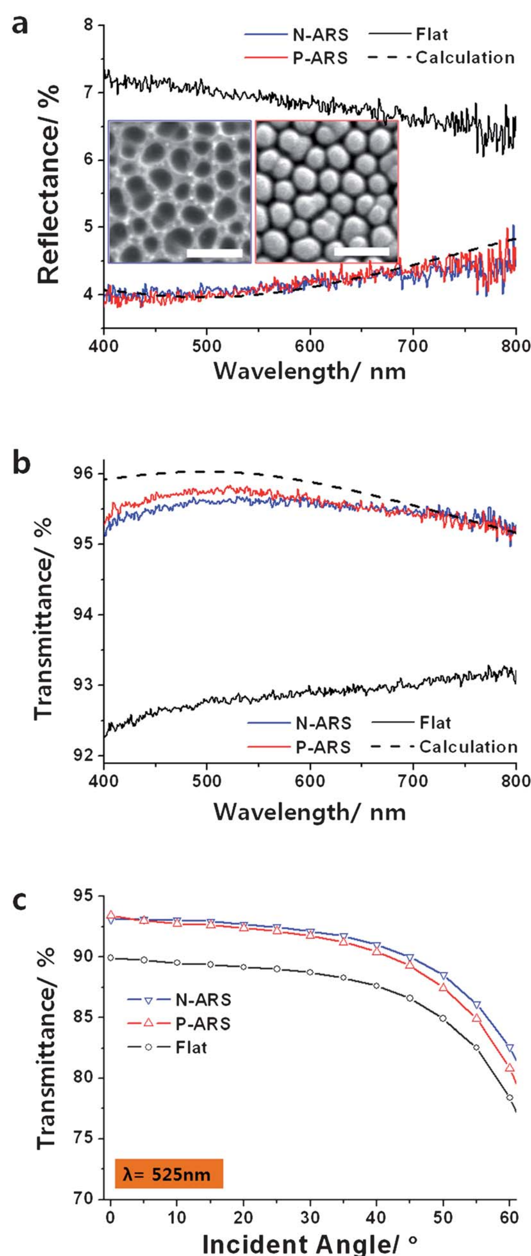

Fig. 4 (a and b) Reflectance and transmittance of visible light through a flat reference film (black solid line) and two AR films with either P-ARS (red line) or N-ARS (blue line) on only one surface. The calculated values are also included (black dashed line). SEM images showing N-ARS and P-ARS are also shown. (c) Transmittance of a 525 nm wavelength through a flat reference film, P-ARS, and N-ARS films as a function of the incidence angle. The data in (a and b) were obtained with an integrating sphere and the data in (c) were obtained without an integrating sphere.

measured. This behavior would be extremely useful for the application of an AR film to many optical devices, such as solar cells and flat panel display units, which require high transmittance at various incidence angles.[13,31,32]

Fig. 5 presents the reflectance of the N-ARS film and flat PMMA film. The film on the left-hand side is a N-ARS film with porous ARS structures on both surfaces and the one on the

Fig. 5 Digital images of an AR film with N-ARS on both surface (left) and the reference flat film on the LCD monitor of a notebook computer.

right-hand side is the flat film. Both films were placed on the LCD monitor of a notebook computer. Although the flat film appeared to be opaque due to surface reflection, the N-ARS film was clear and transparent.

2.4. Mechanical stability of ARS

The mechanical stabilities of N-ARS and P-ARS were tested by monitoring the change in transmittance after the two films had been pressed mechanically with the given normal pressure. Fig. 6 shows the fractional transmittance ($f_T = (T - T_{flat})/(T_o - T_{flat})$), which is the ratio of the transmittance difference between the pressed sample (T) and flat sample (T_{flat}) to that between the initial un-pressed sample (T_o) and flat sample, as a function of the applied stress for the N-ARS and P-ARS samples. After applying a stress of up to 4.2 MPa, both samples maintained a fractional transmittance (f_T) of approximately 0.9. In the case of the P-ARS film, f_T begins to decrease rapidly upon further increases in applied stress, and its value reached approximately 0.4 at 14 MPa pressure. On the other hand, in the case of the N-ARS film, approximately 0.9 of f_T remained at 14 MPa pressure. As expected, the N-ARS structure showed a considerable increase in mechanical stability, probably due to the "bridge" material in the honeycomb structure connecting the neighboring porous ARSs.

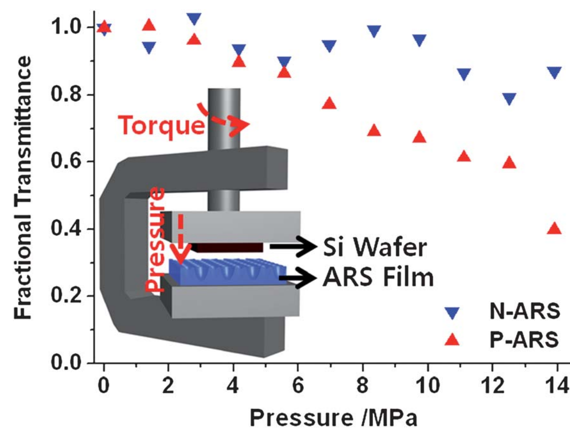

Fig. 6 AR performance change as a function of the applied normal stress for P-ARS and N-ARS films. A schematic diagram showing the accessory used to apply a normal stress is included.

Downloaded by University of Illinois - Urbana on 21 September 2012
Published on 04 July 2012 on http://pubs.rsc.org | doi:10.1039/C2JM32706F

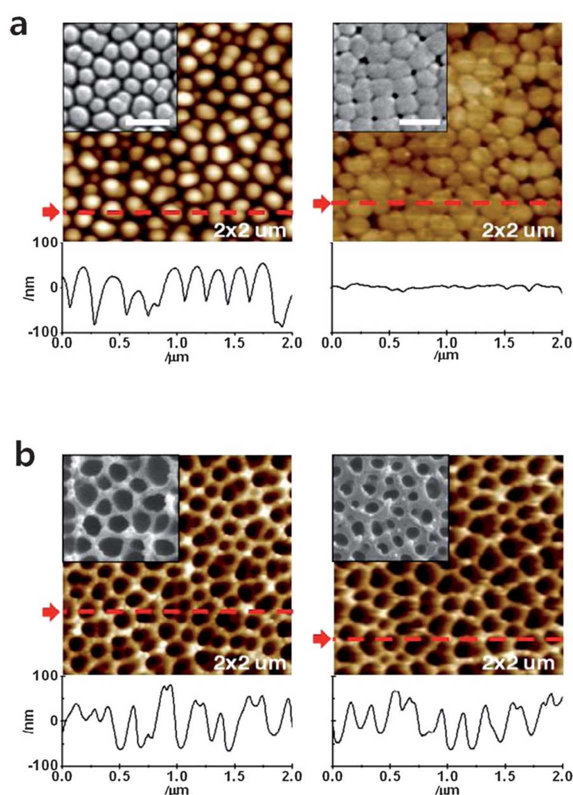

Fig. 7 AFM topographies and height profiles obtained at the position denoted with a red line before (left) and after (right) the application of 14 MPa stress to P-ARS film (a) and N-ARS film (b). Corresponding SEM images are also included in the insets.

The surface morphologies before and after maximum surface stress (14 MPa) had been applied were observed by atomic force microscopy (AFM) (Fig. 7a and b). SEM images are also included inside the AFM images. The topological profiles obtained from a given position denoted with the red arrow in the AFM images are also displayed under the corresponding AFM data. After applying 14 MPa pressure, the P-ARS appears to have been compressed noticeably resulting in a significant change in surface morphology. On the other hand, N-ARS appears to maintain most of its initial structure. This difference between P-ARS and N-ARS can be also confirmed from the SEM data and topological profiles. Overall, the AR film based on the N-ARS showed much higher mechanical stability than the corresponding one based on the P-ARS, even though both AR films exhibit similar AR performance.

3. Conclusion

In this study, an AR polymer film based on a negative nanoporous structure was fabricated efficiently using a roll-to-roll processable, thermal nanoimprint lithography method. A high performance AR could be achieved by nanotailoring the surface profiles of N-ARS and P-ARS using a multistep anodization process to have a similar linear RI profile in the interphase layer. Furthermore, the AR properties of the N-ARS film were confirmed to be broadband and omnidirectional. Compared to the conventional P-ARS structure, the N-ARS in a honeycomb pattern was found to maintain high AR performance with little structural deformation under strong compressive stress. This study suggests a new type of ARS and its fabrication process, which can be utilized in the industrial production of flexible AR films. The mechanical stability of many nano-devices might be enhanced significantly by applying the well-established technologies of macroscopic structure physics to nanoscale structure physics.

4. Experimental section

4.1. Roller mold fabrication

For the fabrication of the PI mold shown in Fig. 3c, poly(amic acid) (PAA) (Aldrich) was used as a PI precursor and was dissolved in *N*-methyl pyrrolidone (NMP) to produce a 15–16 wt% solution. The PAA solution was then dropped onto the AAO surface to infiltrate the PI solution into the negative pores in AAO *via* template wetting.[33–35] Upon further spin coating of the PAA solution on AAO (4000 rpm, 1 min), the AAO was placed in a furnace (TF-150VG, Intec) under a nitrogen atmosphere. The furnace was then heated to 100 °C at a heating rate of 5°C min^{-1} and maintained for 20 min to remove the NMP solvent. The PAA infiltrated AAO was then cured on a hot plate at 150 °C for 30 min, followed by heating at 200 °C for 30 min, and then at 250 °C for 60 min under nitrogen. A PAA solution was spin coated twice more (500 rpm, 1 min) on the cured PI/AAO and cured again using the previous curing process. The cured PI film was then detached mechanically from the AAO mold to produce a PI mold (50 mm diameter, 100 µm thickness) with positive ARSs on its surface. The PI mold was wound on a stainless steel roller (41 mm diameter), which had been covered with a 3 mm thick poly(dimethylsiloxane) film to finally prepare the PI roller mold.

4.2. N-ARS fabrication

An approximately 200 µm thick PMMA film was prepared by melting PMMA ($M_w = 100\,000$ g mol^{-1}, Polysciences) at 150 °C for 5 min and then applying a 2000 kgf force with a melt presser (Carver, 2697) between two flat PI films (Kapton JP, DuPont). The pressed film was then quenched in ice water to freeze the shape of the film, and the PI film on one side of the PMMA film was then removed. As shown in Fig. 3e, PMMA with a PI film on one side was placed on a hot plate. After heating the PMMA film to 150 °C, the PI roller mold prepared above was placed on an edge of the PMMA film. The roller mold was then pressed against and rotated on the PMMA film surface. Any air bubbles that formed between PMMA film and PI roller mold could be removed during thermal nanoimprint lithography. The PMMA film with the N-ARSs imprinted on its surface was then cooled immediately below its glass transition temperature by blowing cold air before being detached mechanically from the PI roller mold. The PMMA film with N-ARS on its surface could be fabricated by removing the remaining flat PI film.

4.3. Optical simulation

The reflection spectra in the visible wavelength range (λ = 400–800 nm) were calculated using RCWA for the ARS with a

 This journal is © The Royal Society of Chemistry 2012

Downloaded by University of Illinois - Urbana on 21 September 2012
Published on 04 July 2012 on http://pubs.rsc.org | doi:10.1039/C2JM32706F

linear RI profile. In the RCWA calculation, a five-step graded surface layer from $n_{air} = 1.0$ to $n_{PMMA} = 1.49$ with a step index of $\Delta n = 0.082$ on a PMMA substrate was assumed. Each layer had the same thickness and increased simultaneously as the total height was increased from 0 to 400 nm. The calculated reflection spectra were similar to that of a nearly linear-graded surface layer with $\Delta n = 0.01$. For simplicity, the dispersion and absorption of a PMMA film were not considered.

4.4. Stress analysis

Finite element (FE) models consisting of 1140 (in P-ARS FE model) and 3054 (in N-ARS FE model) numbers of 20 node iso-parametric brick elements were used for nonlinear elasto-plastic finite element stress analysis using the explicit module of ABAQUS V6.10. For FE analysis, a typical PMMA material stress–strain curve was used. The material density and Poisson ratio used were 1.195 g cm^{-3} and 0.5, respectively.

4.5. Optical measurements

The reflectance and transmittance values in Fig. 4a and b were measured using a spectrophotometer (Perkin-Elmer lambda 650) equipped with an integrating sphere for the wavelength range 400–800 nm at 1 nm intervals. Deuterium and tungsten lamps were the light sources. The reported reflectance and transmittance are the mean values of several datasets obtained from various spots of an identical sample. The transmittance values at different incidence angles shown in Fig. 4c were obtained without an integrating sphere.

4.6. Mechanical stability measurements

A small sized accessory, the schematic of which is shown in Fig. 6, was prepared to apply a normal stress to both AR films. Initially, an AR film was placed on the fixed bottom plate, and a small Si wafer (6×6 mm^2) was attached beneath the movable top plate. The top plate was then lowered by turning the central shaft with a torque wrench. The normal pressure applied was measured using a load cell.

Acknowledgements

The authors wish to thank Prof. Jinsub Choi of Inha University for his contribution to developing the multistep anodization process. This study was supported by the Basic Science Research Program through the National Research Foundation of Korea (NRF) funded by the Ministry of Education, Science and Technology (Grant 2010-0024153).

Notes and references

1 Y. Huang, S. Chattopadhyay, Y. Jen, C. Peng, T. Liu, Y. Hsu, C. Pan, H. Lo, C. Hsu, Y. Chang, C. Lee, K. Chen and L. Chen, *Nat. Nanotechnol.*, 2007, **2**, 770.
2 H. E. Jeong, J. Lee, H. N. Kim, S. H. Moon and K. Y. Suh, *Proc. Natl. Acad. Sci. U. S. A.*, 2009, **106**, 5639.
3 A. Tuteja, W. Choi, M. Ma, J. M. Mabry, S. A. Mazzella, G. C. Rutledge, G. H. McKinley and R. E. Cohen, *Science*, 2007, **318**, 1618.
4 R. A. Potyrailo, H. Ghiradella, A. Vertiatchikh, K. Dovidenko, J. R. Cournoyer and E. Olson, *Nat. Photonics*, 2007, **1**, 123.
5 V. A. Ganesh, H. K. Raut, A. S. Nair and S. Ramakrishna, *J. Mater. Chem.*, 2011, **21**, 16304.
6 D. Poitras and J. A. Dobrowolski, *Appl. Opt.*, 2004, **43**, 1286.
7 S. Chattopadhyay, Y. F. Huang, Y. J. Jen, A. Ganguly, K. H. Chen and L. C. Chen, *Mater. Sci. Eng., R*, 2010, **69**, 1.
8 Y. Li, J. Zhang and B. Yang, *Nano Today*, 2010, **5**, 117.
9 D. G. Stavenga, S. Foletti, G. Palasantzas and K. Arikawa, *Proc. R. Soc. London, Ser. B*, 2006, **273**, 661.
10 K. Choi, S. H. Park, Y. M. Song, Y. T. Lee, C. K. Hwangbo, H. Yang and H. S. Lee, *Adv. Mater.*, 2010, **22**, 3713.
11 X.-X. Fu, X.-N. Kang, B. Zhang, C. Xiong, X.-Z. Jiang, D.-S. Xu, W.-M. Du and G.-Y. Zhang, *J. Mater. Chem.*, 2011, **21**, 9576.
12 Y. Li, J. Zhang, S. Zhu, H. Dong, F. Jia, Z. Wang, S. Zhiqiang, L. Zhang, Y. Li, H. Li, W. Xu and B. Yang, *Adv. Mater.*, 2009, **21**, 4731.
13 C. O'Dwyer, M. Szachowicz, G. Visimberga, V. Lavayen, S. B. Newcomb and C. M. Sotomayor Torres, *Nat. Nanotechnol.*, 2009, **4**, 239.
14 L. Li, T. Zhai, H. Zeng, X. Fang, Y. Bando and D. Golberg, *J. Mater. Chem.*, 2011, **21**, 40.
15 R. Lakes, *Nature*, 1993, **361**, 511.
16 Z. W. Shan, G. Adesso, A. Cabot, M. P. Sherburne, S. A. Syed Asif, O. L. Warren, D. C. Chrzan, A. M. Minor and A. P. Alivisatos, *Nat. Mater.*, 2008, **7**, 947.
17 J. Hohe and W. Becker, *Appl. Mech. Rev.*, 2002, **55**, 61.
18 W. H. J. Southwell, *J. Opt. Soc. Am. A*, 1991, **8**, 549.
19 M. G. Moharam and T. K. Gaylord, *J. Opt. Soc. Am.*, 1981, **71**, 811.
20 O. C. Zienkiewicz, *The Finite Element Method*, McGraw-Hill, Maidenhead, 3rd edn, 1977.
21 S. H. Ahn and L. J. Guo, *ACSNano*, 2009, **3**, 2304.
22 D. Suh, S.-J. Choi and H. H. Lee, *Adv. Mater.*, 2005, **17**, 1554.
23 L. J. Guo, *Adv. Mater.*, 2007, **19**, 495.
24 H. Schift, *J. Vac. Sci. Technol., B: Microelectron. Nanometer Struct.–Process., Meas., Phenom.*, 2008, **26**, 458.
25 R. Maboudian and R. T. Howe, *J. Vac. Sci. Technol., B: Microelectron. Nanometer Struct.–Process., Meas., Phenom.*, 1997, **15**, 1.
26 J. Li, C. Li and X. Gao, *Appl. Surf. Sci.*, 2011, **257**, 10390.
27 M. Steinhart, J. H. Wendorff, A. Greiner, R. B. Wehrspohn, K. Nielsch, J. Schilling, J. Choi and U. Gösele, *Science*, 2002, **296**, 1997.
28 J. Jang, K. J. Lee and Y. Kim, *Chem. Commun.*, 2005, 3847.
29 S. Choi, P. J. Yoo, S. J. Baek, T. W. Kim and H. H. Lee, *J. Am. Chem. Soc.*, 2004, **126**, 7744.
30 M. J. Lee, N. Y. Lee, J. R. Lim, J. B. Kim, M. Kim, H. K. Baik and Y. S. Kim, *Adv. Mater.*, 2006, **18**, 3115.
31 J. Zhu, C. Hsu, Z. Yu, S. Fan and Y. Cui, *Nano Lett.*, 2010, **10**, 1979.
32 M. Park, G. Yu and K. Shin, *J. Cryst. Growth*, 2011, **326**, 28.
33 B. G. Park, K. Choi, C. J. Jo and H. S. Lee, *Soft Matter*, 2012, **8**, 1751.
34 M. Zhang, P. Dobriyal, J.-T. Chen and T. P. Russell, *Nano Lett.*, 2006, **6**, 1075.
35 M. Steinhart, R. B. Wehrspohn, U. Gösele and J. H. Wendorff, *Angew. Chem., Int. Ed.*, 2004, **43**, 1334.